Low-activity Main-belt Comet 133P/Elst-Pizarro: New Constraints on Its Albedo, Temperature, and Active Mechanism from a Thermophysical Perspective

Liang Liang Yu (余亮亮)[1] , Chih Hao Hsia[1], and Wing-Huen Ip[1,2]

[1] State Key Laboratory of Lunar and Planetary Sciences, Macau University of Science and Technology, Macau, People's Republic of China; yullmoon@live.com
[2] Institute of Astronomy, National Central University, Jhongli, Taoyuan City 32001, Taiwan

Abstract

133P/Elst-Pizarro is the first recognized main-belt comet, but we still know little about its nucleus. First we use mid-infrared data of *Spitzer* MIPS, *Spitzer* IRS, and the *Wide-field Infrared Survey Explorer* to estimate its effective diameter, $D_{eff} = 3.9^{+0.4}_{-0.3}$ km, geometric albedo, $p_v = 0.074 \pm 0.013$, and mean Bond albedo $A_{eff,B} = 0.024 \pm 0.004$. The albedo is used to compute 133P's temperature distribution, which shows significant seasonal variation, especially polar regions, ranging from ~ 40 to ~ 200 K. Based on current activity observations, the maximum water gas production rate is estimated to be $\sim 1.4 \times 10^{23}$ s^{-1}, being far weaker than $\sim 10^{26}$ s^{-1} of JFC 67P at a similar heliocentric distance of ~ 2.7 au, indicating a thick dust mantle on the surface to lower down the gas production rate. The diameter of the sublimation area may be $< \sim 200$ m according to our model prediction. We thus propose that 133P's activity is more likely to be caused by sublimation of a regional near-surface ice patch rather than a homogeneous buried ice layer. Such a small near-surface ice patch might be exposed by one impact event, before which 133P may be an extinct comet (or ice-rich asteroid) with an ice layer buried below ~ 40 m depth. The proposed ice patch may be located somewhere within latitude $-50 \sim 50°$ by comparing theoretical variation of sublimation temperature to the constraints from observations. The timescale to form such a thick dust mantle is estimated to be > 100 Myr, indicating that 133P may be more likely to be a relatively old planetesimals or a member of an old family than a recently formed fragment of some young family.

1. Introduction

133P/Elst-Pizarro (hereafter 133P) was originally discovered as an asteroid-like point source with no special characteristics in the main belt by the Siding Spring 1.2 m telescope on 1979 July 24, when it was at a mean anomaly of $\sim 15°.3$, thus being named as asteroid 1979 OW7 (McNaught et al. 1996). McNaught et al. (1996) also reported that this object was still a point source on 1985 September 15, when it was at a mean anomaly of $\sim 48°.4$. Then on 1996 August 7, Eric W. Elst and Guido Pizarro observed a main-belt object showing a long narrow dust tail but no gas feature from the ESO 1 m Schmidt telescope at La Silla Observatory. This special object looked like a comet, and thus was designated as comet P/1996 N2, which turned out to be the already discovered main-belt asteroid 1979 OW7. Subsequently the object obtained its current name 133P/Elst-Pizarro.

The phenomenon that 133P suddenly showed comet-like dust tail but no observable gas coma or gas tail is quite strange for a main-belt object with the Tisserand parameter $T_J = 3.18 > 3$, because typical comets like Jupiter family comets (JFCs) as well as Halley family comets (HFCs) have $T_J < 3$. If the observation in 1979 and 1985 did tell us that 133P was an inactive asteroid at that time, then the activity observed on 1996 August 7, when 133P was at a mean anomaly of $\sim 25°.2$, seems to be triggered suddenly at some particular time between 1985 and 1996. For instance, Toth (2000) proposed that the dust tail of 133P was caused by a recent impact event, which could disturb the surface and generate the ejection of surface dust material.

Hsieh et al. (2004) reported the recurrent dust activity of 133P in its 2002 perihelion passage, which lasted at least 5 months

from 2002 August to December based on observations by the UH 2.2 m telescope in 2002 and the Keck I 10 m telescope in 2003, the hypotheses of dust ejection by an one-time impact event to explain the appearance of 133P's comet-like tail in 1996 was thus ruled out. Hsieh et al. (2004) considered a variety of mechanisms to explain the observed comet-like behavior of 133P, but preferred to explain the dust tail of 133P to be the result of seasonal sublimation of exposed surface ice, raising the interesting question about when 133P would be comet-like active and when it would be inactive along its orbit.

For this purpose, Hsieh et al. (2010) carried out a multi-year monitoring campaign of 133P from 2003 to 2008 (nearly an orbital cycle of 133P), and again observed the return of its activity in 2007. They found that 133P looks like an asteroid at most part of its orbit, but can also display a dust tail feature like a comet when it was close to or shortly after perihelion in 1996, 2002, and 2007. Moreover, the recurrence of the dust-tail activity of 133P near perihelion was also observed on 2013 July 10 by the *Hubble Space Telescope* (Jewitt et al. 2014). Such significant seasonal variation and cyclical recurring activity strongly support the idea that the dust ejection activity is caused by ice sublimation, and further imply that there should even exist groups of icy small bodies in the main belt, which led to the discovery of a new comet group, named main-belt comets (MBC; Hsieh & Jewitt 2006).

Hsieh et al. (2004, 2010) tended to explain the recurring activity of 133P by seasonal sublimation of a regional surface icy patch, which may be exposed by impacts from a deeply buried icy layer. This model seemed to be perfect at that time. However, following the discovery of more and more main-belt comets, Hsieh et al. (2015) found that nearly all of the known MBCs, appeared to show activity close to or shortly after perihelion. If sublimation of a regional surface icy patch is

responsible for this observed activity, there is no reason to expect that all the exposed icy patches on these MBCs to get local summer close to or shortly after perihelion, because impacts on the surface should be random events. Therefore, Hsieh et al. (2015) proposed another possible mechanism. That is variation of the sublimate rate of a homogenous buried icy layer due to change of the heliocentric distance may be the cause. A new question thus arises on whether activities of MBCs are caused by the sublimation of regional surface ice patches or by the sublimation of homogenous buried ice layer. The question is quite important, because for such two cases, the thickness of dust mantle on the surface will be different, thus would indicate different age, origin and evolution history.

On the other hand, the discovery of MBCs implies that water ice can survive in the main belt even today since their formation. Details of the physical properties of the MBC nuclei can give us key information about the formation and evolution of the main belt, and hence provide clues about the formation and evolution of the solar system. Clarification of this issue would also shed light on the origin of water on terrestrial planets like our Earth. However, distances to MBCs are too far away for current telescopes to figure out what happens on such MBC nuclei. So a spacecraft mission to MBCs would be necessary and meaningful. This is the reason why 133P becomes the target of a proposed ESA spacecraft mission named "Castalia" (Snodgrass et al. 2018), and it was also selected to be a target of a proposed Chinese small-body mission named "ZhengHe" (Zhang et al. 2019). Thus theoretical modeling and constraints about the thermal environment and thermal activity prior to the space mission would be of significance for both the mission planning and instruments design.

In this paper, we aim to figure out the active mechanism of 133P, and estimate its albedo, temperature, and gas/dust production rate. To realize these goals, first we use the radiometric method to infer the albedo and size of the nucleus of 133P, then simulate the possible temperature variation of the surface layers based on the estimated albedo and thermal parameters. Finally a dust–ice two-layer sublimation model of buried ice is utilized to explain the current available observations on the activity of 133P, which enables us to depict the possible distribution of ice on 133P and the orientation of 133P's rotation axis as well. The results show that the activity of 133P is more likely to be caused by the sublimation of exposed regional near-surface ice patches than a homogenous buried icy layer.

2. Radiometric Constraints

2.1. Thermal Infrared Observations

2.1.1. Spitzer MIPS Data

The Multiband Imaging Photometer on *Spitzer* (MIPS; Rieke et al. 2004) observed 133P/Elst-Pizarro using a 24 μm channel at three different epochs on 2005 April 11 under program 3119 (PI: W. T. Reach). The angular resolution of the MIPS camera at the 24 μm band was 2″.5 with a field of view (FOV) of $\sim$5′.4 × 5′.4. The integrated fluxes for the 24 μm channel are measured using the method described in Hsia & Zhang (2014). The aperture calibrations of this MBC at 24 μm vary in the adopted aperture radii. We have corrected the fluxes using the aperture- and color-calibration factors suggested by the MIPS Instrument Handbook.[3]

The photometric uncertainties of these flux measurements for the 24 μm band are estimated to be from $\sim$7% to 9%. These values of the uncertainties are derived from the absolute flux calibrations and standard deviations of the flux determinations associated with our aperture photometry method. The data are listed in Table 1.

2.1.2. Spitzer IRS Spectrum

The mid-infrared spectra of MBC 133P/Elst-Pizarro were obtained by the *Spitzer* Infrared Spectrograph (IRS; Houck et al. 2004) through the observation program 88 (PI: D. Cruikshank) with the astronomical observation request (AOR) key of 4870400. The data were all obtained on 2006 January 23. The measurements were observed using the short-low (SL) module (7.4–14.5 μm) and the long-low (LL) module (14.0–38.0 μm) with spectral dispersions of $R \sim 60$–130. The diaphragm sizes are 3″.7 × 57′ and 10″.5 × 168′ in SL and LL modules respectively. The total integration times of IRS observation ranged from 968 to 1220 s.

Data were reduced starting with basic calibrated data (BCD) from the Spitzer Science Center's pipeline version s18.7.0 and were run through the IRSCLEAN program to remove bad data points. Then the SMART analysis package (Higdon et al. 2004) was used to extract the spectra. To improve the signal-to-noise ratio (S/N) of the IRS observations, the final SL and LL spectra were performed using the combined data. Since the IRS spectrum with short and long wavelength ranges were observed at different epochs, some scaling is needed for the shorter wavelength observations. We scaled the IRS SL observations by a factor of 1.83 and were able to obtain a smooth spectrum. The journal of IRS spectroscopic observations is summarized in Table 1.

2.1.3. Wide-field Infrared Survey Explorer Data

The *Wide-field Infrared Survey Explorer* (*WISE*) mission has mapped entire sky in four bands at 3.4, 4.6, 12, and 22 μm with resolutions from 6″.1 to 12″. All four bands were imaged simultaneously, and the exposure times were 7.7 s in 3.4 and 4.6 μm and 8.8 s in 12 and 22 μm. A mid-infrared imaging observation of 133P was obtained from the 12 μm band and processed with the initial calibration and reduction algorithm.

The aperture photometry for this object was performed using the same method described in Hsia & Zhang (2014). We adopted the color correction on the calibrated flux for the *WISE* 12 μm band using the color-correction factor given by Wright et al. (2010). To estimate the uncertainties in flux, the standard deviations of the background-subtracted flux measurements were adopted. If we take into account the characteristic uncertainty of the flux measurement, the flux error is estimated to be about 22% for the 12 μm channel. Details of the *WISE* infrared photometric results are also given in Table 1.

2.2. Albedo and Size from NEATM

It is lucky that the thermal infrared observations above were all taken when 133P was far away from its perihelion and did not show observable activity, thus it is safe for us to use them as the thermal emission from the surface of 133P's nucleus, which can be used to derive the albedo, size, and even thermal inertia of the nucleus. However, the orientation of 133P's rotation axis is still unclear yet, so it is not appropriate to use the so-called thermophysical model (TPM; Lagerros 1996) or

---

[3] http://irsa.ipac.caltech.edu/data/SPITZER/docs/mips/mipsinstrumen thandbook/1/

Table 1
Mid-infrared Observations of 133P

UT	MA (°)	r_{helio} (au)	Δ_{obs} (au)	α (°)	Wavelength (μm)	Flux[f] (mJy)	Observatory Instrument
2005 Apr 11 08:01	−139.84	3.573	3.006	14.52	24.0	5.82 ± 0.41	Spitzer/MIPS
2005 Apr 11 08:04	−139.84	3.573	3.006	14.52	24.0	5.50 ± 0.47	Spitzer/MIPS
2005 Apr 11 08:08	−139.84	3.573	3.006	14.52	24.0	5.42 ± 0.43	Spitzer/MIPS
2006 Jan 23 14:20	−89.54	3.259	3.174	17.93	7.4–14.5	⋯	Spitzer/IRS
2006 Jan 23 14:40	−89.54	3.259	3.174	17.93	14.0–21.7	⋯	Spitzer/IRS
2006 Jan 23 15:05	−89.54	3.259	3.174	17.93	19.0–38.0	⋯	Spitzer/IRS
2010 Mar 17 06:21	175.51	3.662	3.419	15.67	W3 (12.0)	2.02 ± 0.45	WISE

Notes. MA: represents the mean anomaly of 133P at the time of observation. α: solar phase angle—the angle between the vector of 133P to the Sun and the vector of 133P to the telescope. f: the Spitzer/IRS spectra contain too many data sets, so we do not list them in this table.

the advanced thermophysical model (ATPM; Rozitis & Green 2011) to explain these data. Nevertheless, we can still estimate the albedo and size of the nucleus from these data via the so-called near-Earth asteroid thermal model (NEATM; Harris 1998).

The nucleus of 133P may have an irregular shape, but the available data cannot resolve the shape in detail. So here, to estimate the size of 133P, we define the effective diameter D_{eff} by treating it to be spherical. Then D_{eff} can be related to its geometric albedo p_v and absolute visual magnitude H_v via (Fowler & Chillemi 1992)

$$D_{eff} = \frac{1329 \times 10^{-H_v/5}}{\sqrt{p_v}} \text{ (km).} \quad (1)$$

On the other hand, the Bond albedo $A_{eff,B}$ can be related to the geometric albedo p_v by

$$A_{eff,B} = p_v q_{ph}, \quad (2)$$

where q_{ph} is the phase integral that can be approximated by

$$q_{ph} = 0.290 + 0.684G, \quad (3)$$

in which G is the slope parameter in the H, G magnitude system of Bowell et al. (1989). The absolute visual magnitude H_v and slope parameter G of 133P have been measured by Hsieh et al. (2010) to be $H_v = 15.49 \pm 0.05$, $G = 0.04 \pm 0.05$, which will be used in our fitting procedure.

The NEATM fitting results are presented in Figure 1, which is a contour of the reduced χ_r^2 with effective diameter D_{eff} and beaming parameter η as two free parameters. The 1σ-level result is not that good, so we will adopt the 3σ-level results $D_{eff} = 3.9^{+0.4}_{-0.3}$ km, $\eta = 1.35^{+0.3}_{-0.2}$. Then the geometric albedo can be derived to be $p_v = 0.074 \pm 0.013$, and the bond albedo can be obtained as $A_{eff,B} = 0.024 \pm 0.004$, which would be useful for TPM. To verify the results, we plot the comparison between the Spitzer IRS spectra and best-fit curve by NEATM in Figure 2. The best-fit curve by NEATM matches well to the Spitzer IRS spectra, indicating that our radiometric results should be reliable. We summarize the radiometric results in Table 2.

3. Temperature Constraints

Information about the temperature environment of 133P is crucial for the design of instruments on board the spacecraft, especially for the instruments on a lander. The temperature distribution of a small body is largely decided by its rotation and orbital motion. But unfortunately, the exact orientation of
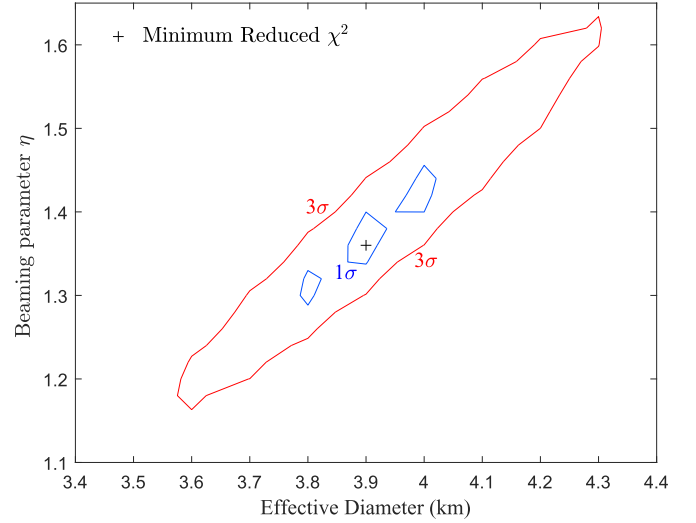

Figure 1. NEATM fitting to the thermal infrared date with effective diameter and beaming parameter as two free parameters. The 1σ boundary (blue curve) corresponds to $\chi^2 = 2.3$, while the 3σ boundary (red curve) corresponds to $\chi^2 = 11.8$ (Press et al. 2007).
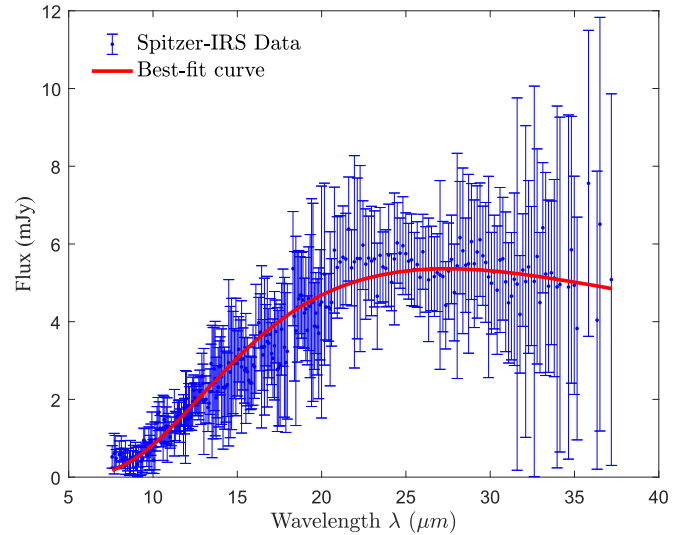

Figure 2. Comparison between the Spitzer IRS spectra and best-fit curve by NEATM with $D_{eff} = 3.9$ km, $\eta = 1.35$, $p_v = 0.074$, and $A_{eff,B} = 0.024$.

133P's rotation axis is still unknown, due to the difficulty of the observation of its light curves when it is inactive. Nevertheless, the temperature environment can still be investigated by considering various cases of orientations of the rotation axis.

Table 2
Derived Results from NEATM Fitting

Properties	3σ Level
Beaming parameter η	$1.35^{+0.3}_{-0.2}$
Effective diameter D_{eff}	$3.9^{+0.4}_{-0.3}$ km
Geometric albedo p_v	0.074 ± 0.013
Bond albedo $A_{\text{eff,B}}$	0.024 ± 0.004

3.1. Description of Rotation Axis

To begin with, we need a coordinate system to give descriptions of the rotation axis. For convenience, we introduce two parameters, obliquity γ and azimuth ν, to define the orientation of the rotation axis with respect to the orbital plane as shown in Figure 3.

Although the exact orientation of rotation axis of 133P is not clear yet, Toth (2006) and Hsieh et al. (2010) have obtained constraints for the obliquity γ according to observed light curves in 2002 and 2007. They found that obliquity $\gamma = 30° \pm 10°$ can fit better to the observed light curves, but the azimuth ν cannot be well constrained.

3.2. Annual Average Temperature

With an assumed value for the obliquity γ, the first thing that we can do is to estimate the annual average temperature on each local latitude θ of 133P. To do this, we need to assume the infinite thermal inertia, and then the fast-rotating or isothermal latitude model (Lebofsky & Spencer 1990) can be applied. The annual average temperature $\tilde{T}(\theta)$ of each latitude can be simply estimated as

$$(1 - A_{\text{eff,B}})\tilde{L}_s(\theta) = \varepsilon\sigma\tilde{T}(\theta)^4, \tag{4}$$

where $A_{\text{eff,B}}$ is the bond albedo as estimated above, $\varepsilon \sim 0.9$ is the average thermal emissivity, and $\tilde{L}_s(\theta)$ is the annual average incoming solar flux on each latitude and can be estimated via (Ward 1974)

$$\tilde{L}_s(\theta) = \frac{L_\odot}{2\pi^2 a^2 \sqrt{1 - e^2}}$$
$$\times \int_0^{2\pi} \sqrt{1 - (\cos\gamma\sin\theta - \sin\gamma\cos\theta\sin\varphi)^2} \, d\varphi, \tag{5}$$

where $L_\odot = 1361.5 \text{ W m}^{-2}$ is the solar constant, a is the semimajor axis in astronomical units, e is eccentricity, γ is obliquity, θ is latitude, and φ is longitude.

If the rotational parameter $\gamma = 30° \pm 10°$, and with the known orbital elements $a = 3.16$ au, $e = 0.1578$ of 133P, we are able to estimate the annual average temperature on each local latitude, as shown in Figure 4. The annual average temperature can be about $165 \sim 170$ K on the equator, and be about $130 \sim 155$ K on the poles.

With the estimated mean temperature, we will then estimate the thermal parameters of the surface dust layer (hereafter named as dust mantle) of 133P, because thermal parameters including thermal conductivity, specific heat capacity, and thermal inertia are all strong functions of temperature. According to Gundlach & Blum (2013), the thermal conductivity κ of the dust mantle on small bodies can be related to
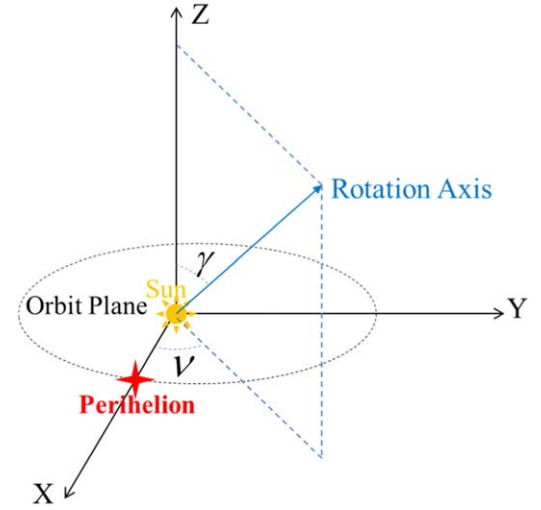

Figure 3. Description of the rotation axis of the small body with respect to its orbital plane. The Z-axis is the normal vector of the orbital plane, the X-axis points from the Sun to the perihelion of the orbit, and the Y-axis is chosen to form a right-handed coordinate system with the Z-axis and X-axis. γ is obliquity and ν is the azimuth angle.
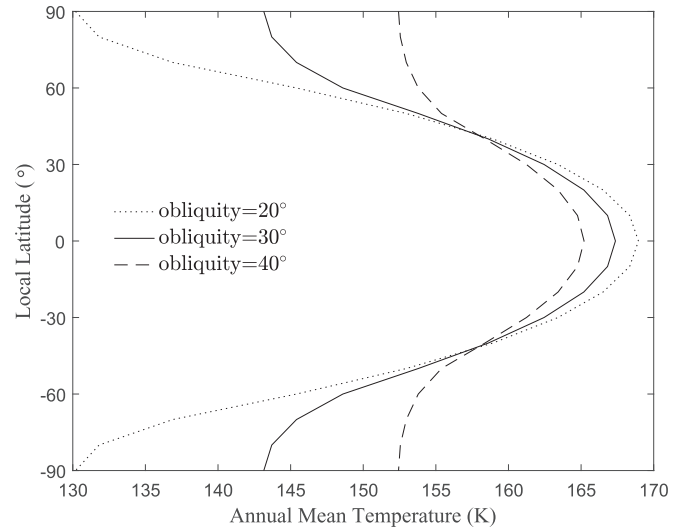

Figure 4. Estimated annual average temperature on each local latitude of 133P on the basis of obliquity $\gamma = 30° \pm 10°$. The so-called local latitude θ is defined as the the complementary angle of the angle between the local normal vector and the rotation axis.

temperature T, mean grain radius b, and porosity ϕ via

$$\kappa(T, b, \phi) = \kappa_{\text{solid}}\left(\frac{9\pi}{4}\frac{1 - \mu^2}{E}\frac{\gamma(T)}{b}\right)^{1/3} \cdot f_1 e^{f_2(1-\phi)} \cdot \chi$$
$$+ 8\sigma\epsilon T^3\frac{e_1\phi}{1 - \phi}b, \tag{6}$$

where $\kappa_{\text{solid}} \sim 1.5 \text{ W m}^{-1}\text{ K}^{-1}$ is the thermal conductivity of the dust material, μ is Poisson's ratio, E is Young's modulus, $\gamma(T)$ is the specific surface energy, ϵ is the emissivity of the material, and f_1, f_2, χ, and e_1 are the best-fit coefficients. For more details, we refer the reader to Gundlach & Blum (2013).

While the range of the grain size of the surface materials may be different for various types of small bodies (especially

inactive asteroids), 133P is expected to be more cometary-like with a dust mantle on the surface. The size frequency distribution of dust on comets is generally described with a power-law formula $f(b) \sim b^{-3.5}$, with minimum to maximum radius b from 0.1 μm to $\sim$1000 μm (Rinaldi et al. 2017). Hsieh et al. (2004), Hsieh & Jewitt (2006), and Jewitt et al. (2014) inferred that dust particles in the observed dust tail of 133P may be mainly $\sim$10 μm in radius. So we may surmise that smaller dust grains with radius from 0.1 μm to tens of micron might have been depleted from most of the surface (not including the newly exposed surface). If removing dust grains <50 μm, dust grains with a radius of 100 ± 50 μm would have a fraction

$$\sim \int_{50}^{150} b^{-3.5} db \Big/ \int_{50}^{1000} b^{-3.5} db \sim 93.64\%$$

of the total leftover dust grains. So we assume that the mean radius of the leftover dust grains on 133P's surface may be mainly 100 ± 50 μm.

Then if considering a annual mean temperature of $\sim$160 K and porosity $\phi \sim 0.5$ of the dust mantle, the mean thermal conductivity of the dust mantle can be estimated from Equation (6) to be $\kappa \sim 1.2 \times 10^{-3}$ W m^{-1} K^{-1}. If further assuming the mean grain density $\rho_d \sim 2000$ kg m^{-3} and mean specific heat capacity to be $c_p \sim 500$ J kg^{-1} K^{-1}, the annual mean thermal inertia Γ of the surface could be estimated to be

$$\Gamma = \sqrt{(1 - \phi)\rho_d c_p \kappa} \sim 25 \text{ J m}^{-2} \text{ s}^{-0.5} \text{ K}^{-1}$$

being close to the thermal inertia of comet nuclei, e.g., 67P (Gulkis et al. 2015). Besides, the mean thermal diffusivity can be estimated as

$$\alpha = \frac{\kappa}{(1 - \phi)\rho_d c_p} \sim 2.4 \times 10^{-9} \text{ m}^{-2} \text{ s}^{-1},$$

and thus the seasonal thermal skin depth can be evaluated as

$$l_{sst} = \sqrt{\frac{\alpha P_{orb}}{2\pi}} \sim 0.3 \text{ m},$$

where P_{orb} is the orbital period of 133P. Although the estimates of these thermophysical parameters are quite rough approximations, they are still useful for further analysis on the thermal behavior of the nucleus of 133P.

3.3. Seasonal Temperature Variation

As noted above, the assumed obliquity of $\gamma \sim 30°$ between the rotation axis and normal vector of the orbital plane can have significant influence on the variation of surface temperature along the orbit. We will show that the azimuth ν defined in Figure 3 can also have significant influence on the seasonal temperature variation.

Since the azimuth ν of 133P is still unclear yet, we consider its value to vary from $-180°$ to $180°$ with a step of $30°$. The simulated results are presented in Figure 5. In each panel of Figure 5, the horizontal axis represents the orbital mean anomaly, the vertical axis is local latitude, and the color index stands for the diurnally averaged surface temperature. Each panel is obtained under the assumption of different azimuth ν of the spin orientation but the same obliquity $\gamma \sim 30°$.

According to Figure 5, we can clearly see that temperature on each local latitude can reach maximum (summer) or minimum (winter) at different orbital positions as a result of seasonal effect. Temperature on the poles can vary from $\sim$40 K to $\sim$200 K. Such seasonal variation can cause similar variation of gas/dust production if there exist near-surface ice. The distribution of ice on 133P can be investigated if we have enough observations on the activity of 133P. In the following section, we will present the available observations at present on the activity of 133P, and what we can learn from these observations.

4. Activity Constraints

4.1. Available Observations

Hsieh et al. (2004, 2010), Jewitt et al. (2014), and Snodgrass et al. (2018) reported optical photometry of 133P along its orbit, showing that activity of the dust tail can appear between a mean anomaly of $\sim -5°.4$ and $\sim 74°$. Hsieh et al. (2010) and Jewitt et al. (2014) also measured the ratio of the light-scattering area of dust C_d to that of nucleus C_n according to the photometric images. In the section above, we have computed the effective diameter D_{eff} of 133P to be about 3.9 km. So if we assume that the dust particles in the tails have similar albedo to that of the nucleus, and have an average radius of $b_d \sim 10$ μm (Hsieh et al. 2004), we could estimate the total dust mass via

$$M_{dust} = \frac{1}{3}\pi \rho_d b_d \frac{C_d}{C_n} D_{eff}^2, \qquad (7)$$

where ρ_d represents the mass density of the dust particles. The values of C_d/C_n and M_{dust} are listed in Table 3 and plotted in Figure 6 as functions of the orbital mean anomaly. The variation of the produced dust mass show significant seasonal variation, which could provide an estimation on the dust production rate, and even the constraints on the distribution of ice on 133P.

4.2. Dust/Gas Production Rate

The slope of the dust–mass variation curve in Figure 6 indicates the production rates of dust, which also vary with the orbital position. We can infer that activity at least starts at around a mean anomaly of $-5°.4$, where the slope of dust mass indicates the total dust production rate of $\sim$0.0017 kg s^{-1} and the total water gas production rate of 1.1×10^{22} s^{-1} if assuming that the dust–ice mass ratio is $\sim$5:1, similar to that of 67P (Fuller et al. 2016). We also find that the slop seems to reach maximum at around $8° \pm 3°$, indicating that 133P may be most active during this time range with a total dust production rate of $\sim$0.0215 kg s^{-1} and a total water gas production rate of 1.4×10^{23} s^{-1}.

The estimation for the maximum water production rate here is consistent with the upper limit of the water production rate $< \sim 10^{24}$ s^{-1} given in Licandro et al. (2011). But such a water production rate is far weaker than that $\sim 10^{26}$ s^{-1} of a typical JFC like 67P at a similar heliocentric distance of $\sim$2.7 au (Hansen et al. 2016), indicating the existence of a dust mantle on the surface, thus lowering down the gas production rate. But the question about how and where the gas is produced from the nucleus of 133P, namely, whether the gas is produced by sublimation from a homogeneous buried ice layer or only from regional near-surface ice patches, is still unsolved. We will discuss such question in the following sections.
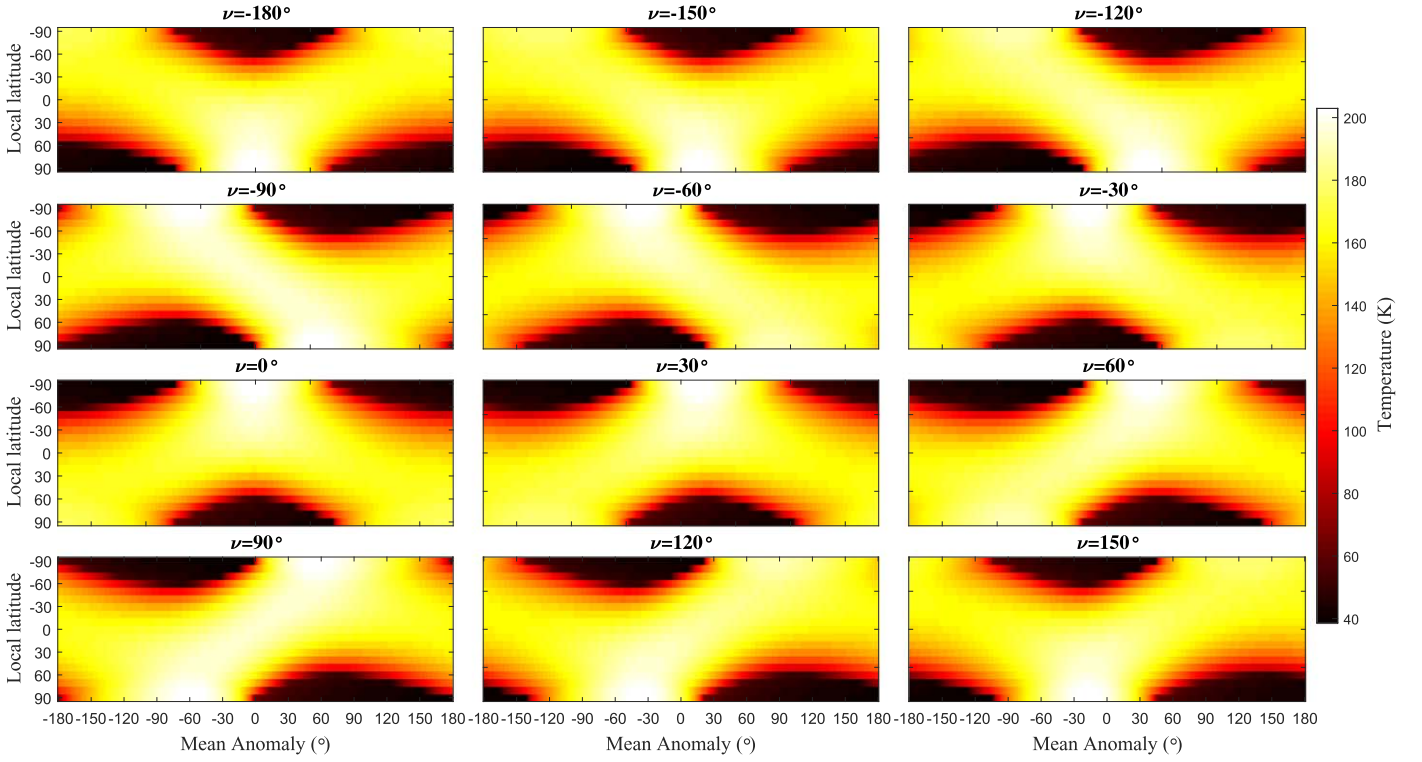
Figure 5. Each panel represents seasonal variation of the diurnally averaged surface temperature as a function of local latitude under the assumption of different azimuth ν of the spin orientation but the same obliquity $\gamma \sim 30°$. For different spin orientation, temperature on different latitude will reach the maximum (summer) or minimum (winter) at different orbital positions, as the result of seasonal effect.

Table 3
Previous Photometry Observations of 133P (Hsieh et al. 2004, 2010; Jewitt et al. 2014)

UT	MA (°)	C_d/C_n	M_{dust} (10^5 kg)
2007 May 19	−5.4	0.20 ± 0.13	0.3186 ± 0.2072
2007 Jul 17	4.9	0.26 ± 0.08	0.4141 ± 0.1274
2007 Jul 20	5.5	0.25 ± 0.08	0.3982 ± 0.1274
2007 Aug 18	10.5	0.61 ± 0.18	0.9716 ± 0.2867
2007 Sep 12	14.9	0.69 ± 0.18	1.0990 ± 0.2867
2013 Jul 10	27.6	0.43 ± 0.07	0.6849 ± 0.1115
2002 Aug 19	51.0	0.21 ± 0.08	0.3345 ± 0.1274
2002 Sep 8	54.5	0.18 ± 0.08	0.2867 ± 0.1274
2002 Nov 6	64.8	0.18 ± 0.08	0.2867 ± 0.1274
2002 Dec 28	74.1	0.20 ± 0.08	0.3186 ± 0.1274
2008 Oct 27	86.8	Faint dust	⋯

Note. MA: represents the mean anomaly of 133P. C_d: light-scattering area of dust. C_n: light-scattering area of nucleus. M_{dust}: Estimated total dust mass if the dust radius is ∼10 μm.

4.2.1. Homogeneous Buried Ice Layer?

If it is assumed that 133P has a homogeneous two-layer system with a dust mantle covering a dust–ice mixture interior. The thickness of the dust mantle should be ∼50–150 m if 133P has stayed in the main belt over the entire lifetime of the solar system according to Prialnik & Rosenberg (2009). For such a two-layer system, the two-layer sublimation model developed in Yu et al. (2019) can be well applicable. But if 133P is a newly formed fragment of a larger icy parent object, the ice layer can be closer to the surface, and the dust mantle can be much thinner. The question is how thin the dust mantle could

be in the case of a homogeneous distribution? If we expect the existence of a stable dust mantle on 133P, the dust mantle thickness is then expected to be several seasonal thermal skin depths, like $2l_{sst} \sim 0.6$ m. Then the two-layer sublimation model (Yu et al. 2019) can still be a good approximation. If adopting the obliquity of 133P to be about $\pm30°$, then the seasonal equilibrium subsurface temperature $\tilde{T}_0$ and corresponding ice sublimation front temperature T_i at each local latitude can be estimated, as shown in left panel of Figure 7.

The right panel of Figure 7 presents the model estimated water sublimation rate of the ice front below each local latitude from 4×10^{12} m^{-2} s^{-1} to 3×10^{15} m^{-2} s^{-1}. The total water gas production rate of such a homogeneous case can be estimated to be $\sim 10^{22-23}$ s^{-1}, which is quite close to the above estimated production rate from observation. Thus we may say that the homogeneous case is reasonable if just considering the total production rate of $< \sim 10^{23}$ s^{-1}.

However, in order to be able to eject dust particles, the drag force of the outflow gas has to overcome the gravity force of the dust particles

$$F_{drag} = C_d \pi b_d^2 \hat{m} \tilde{v}_{th} J_s > \frac{4}{3} \pi b_d^3 \rho_d g_s, \qquad (8)$$

where $\tilde{v}_{th}$ represents the mean thermal velocity of water molecules at the surface, J_s means the outflow number flux at the surface, and

$$g_s \sim \frac{GM}{R^2} - R\omega^2 \cos^2\theta$$

stands for gravitational acceleration at the surface of 133P. As noted above, dust particles in the dust tail are mainly 10 μm in radius (Hsieh et al. 2004, 2010), the outflow water flux is hence
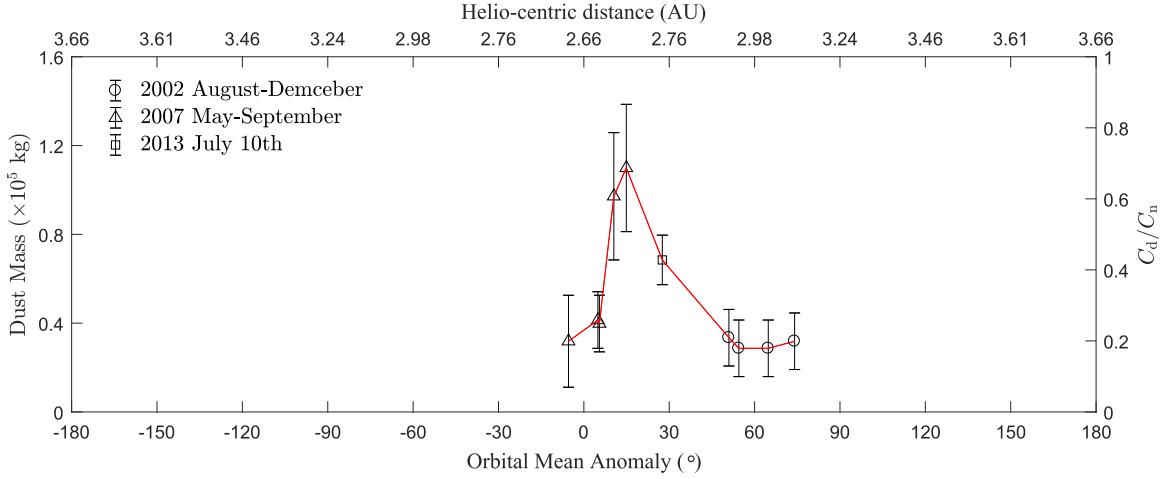
Figure 6. Vertical axis: the ratio of the light-scattering area of dust to that of the nucleus (right side: C_d/C_n) and estimated total dust mass (left side: M_{dust}) based on data in Table 3. The horizontal axis represents the orbital mean anomaly. The variation of the total dust mass shows significant seasonal variation. The slope of the dust–mass variation curve can give us constraints on the dust production rate.
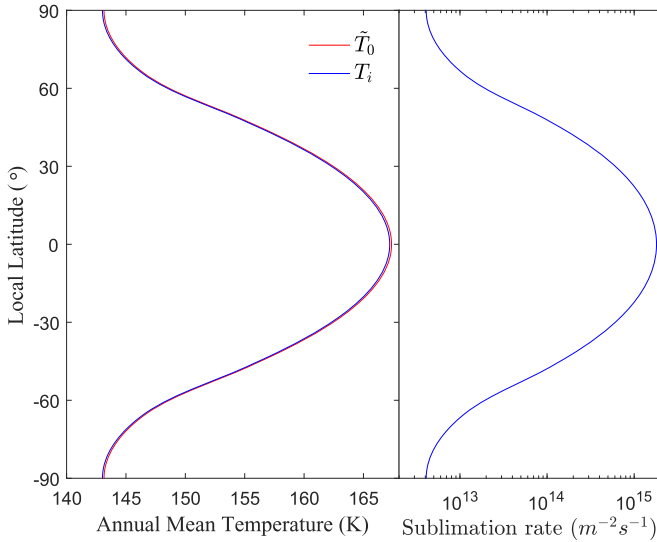

Figure 7. Left panel: equilibrium subsurface temperature $\tilde{T}_0$ of the dust mantle and the ice front temperature T_i at each local latitude; in the case of $\tilde{T}_0 < 180$ K, T_i nearly equals to $\tilde{T}_0$. Right panel: sublimation rate of water ice below each latitude.

required to be $J_s > \sim 5 \times 10^{17} \, \mathrm{m^{-2} \, s^{-1}}$, indicating a sublimation temperature of $T_i > \sim 185$K. So the maximum sublimation rate $\sim 3 \times 10^{15} \, \mathrm{m^{-2} \, s^{-1}}$ of the homogeneous case shown in Figure 7 is too weak to drag away dust particles with a radius $10 \, \mu m$ from the nucleus surface of 133P, although such a homogeneous case can have a similar total water production rate to the observation constraint.

On the other hand, from considering the maximum total water gas production rate of $\sim 10^{23} \, \mathrm{s^{-1}}$, and the requirement of the sublimation rate of $> \sim 5 \times 10^{17} \, \mathrm{m^{-2} \, s^{-1}}$, we can estimate that the sublimation area should be $< \sim 3 \times 10^5 \, \mathrm{m^2}$, corresponding to a circular area with a diameter of $< \sim 600$ m, which is a small region on the surface (nearly $<1/10$ of the total surface of 133P). Therefore, we tend to believe that sublimation of a homogeneous buried ice layer is unlikely to be responsible for the observed activity, and instead a regional near-surface ice patch is necessary to explain the observations.

4.2.2. Regional Near-surface Ice Patch?

So if we expect a near-surface ice patch to be the explanation of the observations, seasonal temperature variation of the ice patch should be responsible for the observed seasonal variation of dust tail activity. The dust activity was observed to start at around a mean anomaly of $-5°.4$, indicating a sublimation temperature of $\sim 180 \pm 5$ K at this orbital position. The estimated total water production rate at around a mean anomaly of $8° \pm 3°$ is nearly 10 times larger than that at a mean anomaly of $-5°.4$. If assuming the sublimation area of the ice patch to be unchanged, the sublimation rate at a mean anomaly of $8° \pm 3°$ would also be 10 times larger, thus giving $J_s > \sim 5 \times 10^{18} \, \mathrm{m^{-2} \, s^{-1}}$, and the sublimation temperature to be around 200 ± 10 K. Then the area of the near-surface ice patch can be estimated to be $< \sim 3 \times 10^4 \, \mathrm{m^2}$, corresponding to a circular area with a diameter $< \sim 200$ m, which is indeed a small region on the surface of 133P. The results for the production rates and sublimation temperature are summarized in Table 4.

If assuming that the possible ice patch is in the bottom of one of the bowl-shaped craters, the diameter of the crater rim has to be on the order of ~ 200 m. Such a small crater can be created from one impact event by an impactor with a diameter of ~ 20 m and an impact velocity of $\sim 10 \, \mathrm{km \, s^{-1}}$ (Vincent et al. 2015). The estimated diameter of the crater rim can further tell us that the depth of the crater should be around ~ 40 m according to the nearly 5:1 ratio of crater rim diameter to crater depth given in Pike (1974). This scenario indicates that the internal ice layer should be buried below ~ 40 m depth from the surface before the impact event. If 133P was initially composed of a homogeneous mixture of dust and water ice, the timescale to form a dust mantle with a thickness of $h_i \sim 40$ m in its current orbit can be estimated as

$$t_m \sim \frac{h_i^2}{2R_r} \tag{9}$$

via the long-term retreating model of a buried ice layer described in Yu et al. (2019), where

$$R_r = \frac{\hat{m} \tilde{\beta} n_E}{(1 - \phi) \rho_d \chi_0}, \tag{10}$$

Table 4
Estimated Dust and Water Gas Production Rate of 133P

	MA (°)	Dust (kg s^{-1})	Water Gas (s^{-1})	Temperature (K)
Start	−5.4	0.0017	1.1×10^{22}	185 ± 5
Maximum	8 ± 3	0.0215	1.4×10^{23}	200 ± 10
Stop	74.1	⋯	⋯	⋯

Note. *: Assuming a dust-to-mass ratio of ∼5:1.

is defined as the retreating rate of the buried ice layer, in which $\hat{m}$ is the mass of the water molecules, $\tilde{\beta}$ is the mean Knudsen diffusion coefficient, n_E is the saturation number density under the temperature T_i of the buried sublimation front, and $\chi_0 \sim 0.15$ is the ice/dust mass ratio. For the current 133P with a mean temperature of $T_i < \sim 165$ K of the buried sublimation front,

$$R_r < \sim 2.6 \times 10^{-13} \text{ m}^2 \text{ s}^{-1},$$

thus giving

$$t_m > \sim 100 \text{ Myr}.$$

Therefore, it can be expected that 133P has been in the main belt for a long time, with the ice layer deeply buried below ∼40 m depth in most regions. This timescale is much larger than the proposed age of ⩽14 Myr (Carruba 2019) of the young Beagle family that is thought to be associated with 133P (Nesvorný et al. 2008), indicating that 133P is more likely to be a relatively old planetesimal or a member of an old family (e.g., Themis family) than a recently formed fragment of a young asteroid family.

If it is assumed that the buried ice layer has a similar dust/ice mass ratio and dust size distribution as those of fresh JFCs, then the sublimation of the exposed ice patch can be active enough to blow away ∼10 μm dust particles and hence generate dust tails like the observations. During the early tens of orbital cycles, the strong sublimation of the ice patch can blow away most dust particles. A very thin dust mantle with a thickness <1 cm may form on the proposed ice patch just like the surface layers of 67P. But such a thin dust mantle would be unstable and can be repeatedly formed and destroyed following the diurnal or orbital cycles, causing a moving boundary and hence preventing the formation of a stable dust mantle until the accumulation of a sufficient amount of large dust particles (>2 cm) on the surface. In this way, the current observation might be explained.

4.3. Possible Location of the Exposed Ice Patch

Now the question of most interest is where the exposed icy patch can be located on the surface. The significant seasonal variation of the activity as shown in Figure 6 should be the result of time variation of the temperature of the near-surface ice patch, thus giving constraints for the sublimation temperature as shown in Table 4. Moreover, temperature on different local latitudes can show different seasonal variations as the result of some particular orientation of rotation axis with respect to the orbit (as shown in Figure 5). This relation would provide a way to investigate the possible location of the surface ice patch and the orientation of the rotation axis. We treat the location latitude LA_i of the possible ice patch and the azimuth ν
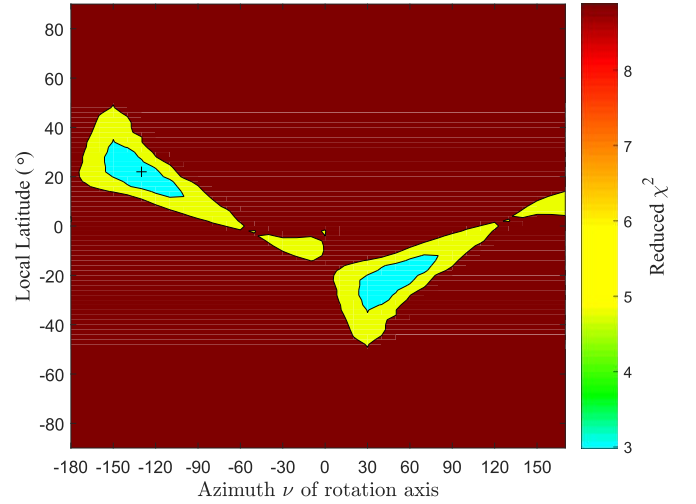

Figure 8. Contour of reduced χ^2 based on fitting to Table 4 with two free parameters—location latitude LA_i of the possible icy patch and the azimuth ν of rotation axis. The black "+" stands for the best-fit result, the cyan region stands for the 1σ-level constraint, and the yellow region represents the 3σ-level constraint.

of the rotation axis as two free parameters to fit the previously obtained values for the sublimation rate and sublimation temperature in Table 4. The fitting results are presented in Figure 8.

Figure 8 shows the contour of reduced χ^2 obtained by fitting LA_i and ν to the sublimation temperature given in Table 4. The location of the lowest reduced χ^2 indicates the best fit to be $LA_i \sim 20°$ and $\nu \sim -130°$. The cyan region stands for 1σ-level constraint for LA_i and ν, giving $LA_i = 10° \sim 40°$, $\nu = -160 \sim -100°$ or $LA_i = -40 \sim -10°$, $\nu = 20 \sim 80°$. The yellow region represents the 3σ-level constraint, giving $LA_i = -50 \sim 50°$ only.

In terms of the 3σ-level contour, the azimuth ν still cannot be well constrained due to the lack information of the seasonal variation of the sublimation rate on 133P from observations. Nevertheless, we can at least infer the location latitude LA_i of the possible ice patch to be between a latitude of $-50 \sim 50°$, indicating that the possible ice patch is unlikely to be located at high latitudes > 50°. If using the best-fit result $LA_i \sim 20°$ and $\nu \sim 130°$ as an example, we can simulate how the sublimation temperature, sublimation rate and hence gas drag force, and total water production rate of the near-surface ice patch vary with orbital movement. The results are presented in Figure 9.

Figure 9 clearly shows how the seasonal variation of sublimation temperature of a regional near-surface ice patch affects the sublimation rate of water and hence the ejection of dust. In such a case, the ratio of the gas drag force to the gravity force on 10 μm dust particles will only be larger than 1 when 133P gets close to perihelion within a short time interval, thus only producing a dust tail during this period. But the total water gas production rate is too low to form an observable gas coma and dust coma, which may be the reason why we only observed long, narrow dust tails behind 133P.

5. Discussion and Conclusion

Although 133P is famous for being the first recognized main-belt comet and has been discovered for ∼40 yr, we still know very little about the physical properties of this object, which is rather disadvantageous if we need to plan a space
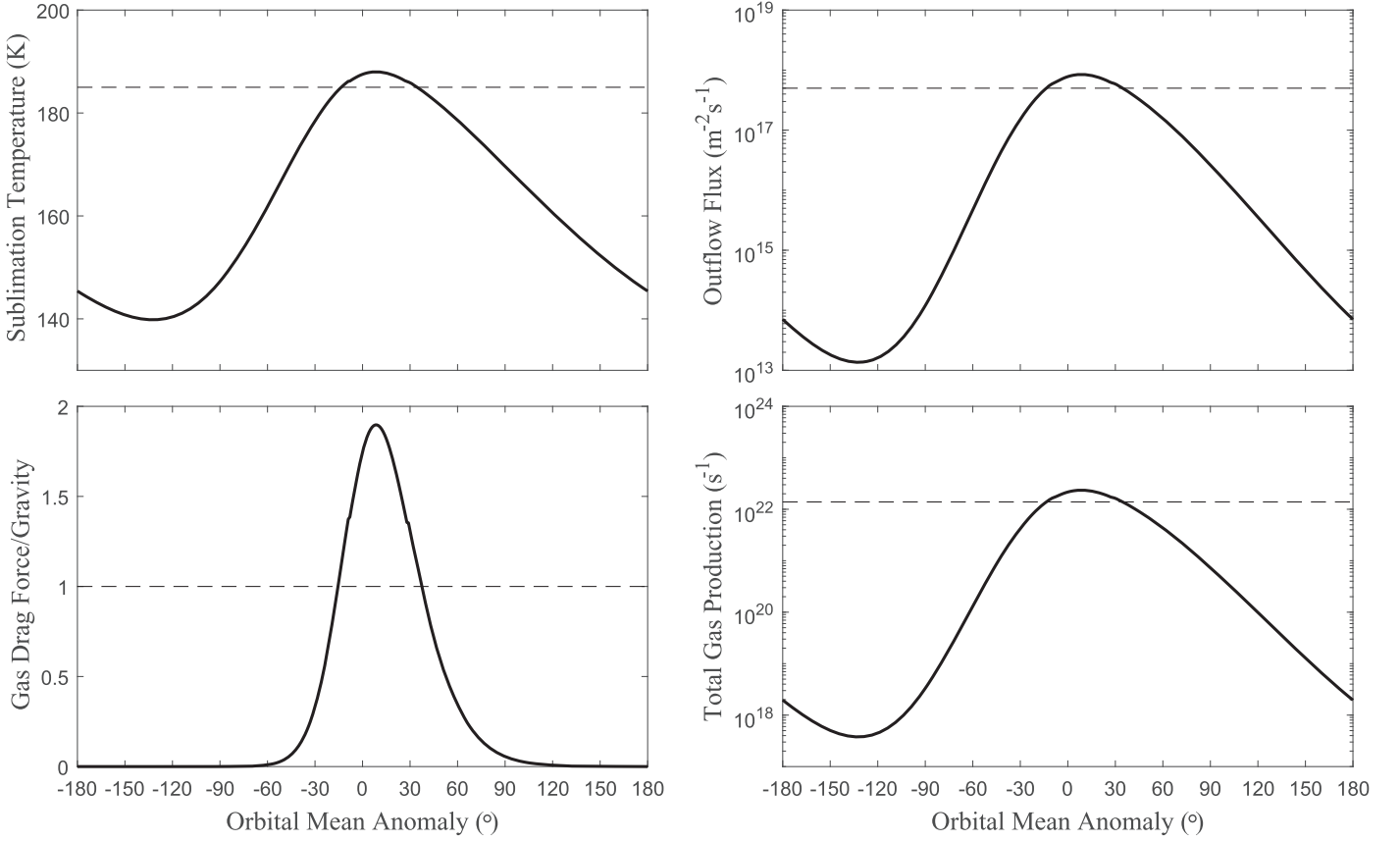
Figure 9. Simulated seasonal variation of the sublimation temperature, outflow flux, ratio of the gas drag force to the gravity force on 10 μm dust particles, and total water production rate assuming a regional near-surface ice patch with a diameter of ∼200 m, located at a latitude of ∼20° of the nucleus that has a rotation axis of $\gamma \sim 30°$ and $\nu \sim -130°$ with respect to the orbital plane of 133P. The horizontal dashed line in each panel represents the critical value when 10 μm dust particles can be ejected.

mission to study it up-close. This paper therefore aims to obtain estimates for the basic physical parameters of 133P, including size, albedo, temperature, and even an activity mechanism. First, by an NEATM fitting to the data from *Spitzer* MIPS, *Spitzer* IRS, and *WISE*, we obtain estimates for the effective diameter $D_{\mathrm{eff}} = 3.9^{+0.4}_{-0.3}$ km, geometric albedo $p_v = 0.074 \pm 0.013$, and mean Bond albedo $A_{\mathrm{eff,B}} = 0.024 \pm 0.004$. The derived diameter is close to the result of Hsieh et al. (2009), which used a similar NEATM procedure but only fitted the *Spitzer* MIPS data by assuming a beaming parameter $\eta \sim 1.0$. The estimated p_v is closer to the result of Bagnulo et al. (2010), which utilized a different method based on a polarization measurement when 133P was active. The advantages of our results in comparison to previous results of Hsieh et al. (2009) and Bagnulo et al. (2010) mainly lie in two aspects. First, the mid-infrared data were all obtained when 133P was far away from perihelion and did not show observable activity, these data are consequently thermal emission from the nucleus of 133P completely without pollution by dust activity. Second, the data cover three different epochs, namely three different solar phase angles, making it possible to remove the degeneracy of the diameter and beaming parameter in the NEATM procedure, and hence simultaneously constrain the diameter (albedo) and beaming parameter.

Of course, the method NEATM we use naturally bears disadvantages that the effects of thermal inertia and rotation axis are not well resolved, which could influence the estimates for size and albedo. However, currently the rotation axis of 133P is unclear yet, making it difficult to use the so-called TPM

to derive size, albedo, and thermal inertia simultaneously. In such a condition, the more reasonable way is first using NEATM to compute size and albedo, and second using albedo to estimate mean temperature, finally using mean temperature to estimate thermal parameters.

Actually, it is unavoidable that we still do not know the rotation axis of 133P, because there are not enough light curves of 133P to do a light-curve inversion procedure. Light curve observations of 133P are too difficult for a small optical telescope due to the far distance and small size of 133P, and it is quite difficult to apply large telescopes to observe 133P. Thus we need other ways to investigate the rotation axis of 133P. As we have done in this work, the seasonal variation of activity could provide us a way to investigate the rotation axis. Since the production rate estimated from current observations is too low in comparison to that of a typical JFC like 67P, the activity of 133P is unlikely to be caused by the sublimation of a homogeneous buried ice layer. We thus believe that the activity of 133P might have been generated by the sublimation of a regional near-surface ice patch. The estimated diameter, $<\sim200$ m, of the proposed ice patch can be generated from one impact event by an impactor with a diameter of ∼20 m and an impact velocity of ∼10 km s^{-1} (Vincent et al. 2015). We know that currently 133P can show activity when it is at a mean anomaly of $-5°.4 \sim 74°.1$. But before 1996 August 7, observations of 133P on 1979 July 24 (mean anomaly ∼15°.3) and on 1985 September 15 (mean anomaly ∼48°.4) did not show activity. Thus it is possible that

the proposed ice patch might have been exposed by one impact event during years 1985–1996.

The seasonal feature that dust activity only appears close to or shortly after perihelion further supports the idea of a regional ice patch. Then the location of the ice patch becomes another unknown problem besides rotation axis, which together decide the seasonal variation of 133P's activity, providing us with a way to investigate the location of the ice patch and the orientation of rotation axis. Based on current activity observations, the 3σ-level constraint for the rotation axis is not good yet, making the solution of ice-patch location nonunique as well. However, if we get sufficient observations on the activity of 133P to describe the seasonal variation of dust or gas production rate in future, we are sure that the rotation axis of the nucleus as well as the location of the possible near-surface ice patch could be well approximated this way. Future observation of 133P is planned with the Lulin Observatory in Taiwan, which has observed activities of some main-belt comets (Shi et al. 2019).

In conclusion, we find that the main-belt comet 133P is largely different from typical JFCs, not only in orbital features but also in the distribution of ice in the nucleus. The current activity of 133P might be retriggered by one impact event during years 1985–1996, before which 133P may have been an extinct comet (or ice-rich asteroid) with an ice layer buried below a $\sim$40 m depth from the surface. The timescale to form such a thick dust mantle by sublimation loss of water is estimated to be >100 Myr, being much larger than the age of the young Beagle family, indicating that 133P is more likely to be formed from an old family than a young one, or probably a relatively old planetesimal survived from the dawn of the solar system. The proposed impact event may expose a regional near-surface ice patch with a diameter of $<\sim$200 m, probably located somewhere between a latitude of $-50 \sim 50°$. The seasonal variation of temperature of the exposed ice patch will thus generate the seasonal feature of activity as shown by current observations.

ORCID iDs

Liang Liang Yu (余亮亮) ⬤ https://orcid.org/0000-0003-4539-9011

References

Bagnulo, S., Tozzi, G. P., Boehnhardt, H., et al. 2010, A&A, 514, A99
Bowell, E., Hapke, B., Domingue, D., et al. 1989, in Asteroids II, ed. R. P. Binzel, T. Gehrels, & M. S. Matthews (Tucson, AZ: Univ. Arizona Press), 524
Carruba, V. 2019, P&SS, 166, 90
Fowler, J. W., & Chillemi, J. R. 1992, The IRAS Minor Planet Survey, Tech. Rep. PL-TR-92-2049 (Phillips Laboratory, Hanscom AF Base, MA)
Fuller, M., Marzari, F., Corte, V. D., et al. 2016, ApJ, 821, 19
Gulkis, S., Allen, M., Allmen, P. V., et al. 2015, Sci, 347, aaa0709
Gundlach, B., & Blum, J. 2013, Icar, 223, 479
Hansen, K. C., Altwegg, K., Berthelier, J.-J., et al. 2016, MNRAS, 462, S491
Harris, A. W. 1998, Icar, 131, 291
Higdon, S. J. U., Devost, D., Higdon, J. L., et al. 2004, PASP, 116, 975
Houck, J. R., Appelton, P. N., Armus, L., et al. 2004, ApJS, 154, 18
Hsia, C.-H., & Zhang, Y. 2014, A&A, 563, A63
Hsieh, H., Denneau, L., Wainscoat, R. J., et al. 2015, Icar, 248, 289
Hsieh, H., & Jewitt, D. 2006, Sci, 312, 561
Hsieh, H., Jewitt, D. C., & Fernández, Y. R. 2004, AJ, 127, 2997
Hsieh, H., Jewitt, D., & Fernández, Y. R. 2009, ApJL, 694, L111
Hsieh, H., Jewitt, D., Lacerda, P., Lowry, S. C., & Snodgrass, C. 2010, MNRAS, 403, 363
Hu, X., Shi, X., Sierks, H., et al. 2017, MNRAS, 469, S295
Huebner, W. F., Benkhoff, J., Capria, M. T., et al. 2006, Heat and Gas Diffusion in Comet Nuclei (Noordwijk: ESA)
Jewitt, D., Ishiguro, M., Weaver, H., et al. 2014, AJ, 147, 117
Lagerros, J. S. V. 1996, A&A, 310, 1011
Lebofsky, L. A., & Spencer, J. R. 1990, in Asteroids II, ed. R. P. Binzel, T. Gehrels, & M. S. Matthews (Tucscon: Univ. Arizona Press), 128
Licandro, J., Campins, H., Tozzi, G. P., et al. 2011, A&A, 532, A65
McNaught, R. H., Hawkins, M. R. S., Marsden, B. G., et al. 1996, IAUC, 6473, 2
Müller, T. G., & Lagerros, J. S. V. 1998, A&A, 338, 340
Nesvorný, D., Bottke, W. F., Vokrouhlický, D., et al. 2008, ApJL, 679, L143
Pike, R. J. 1974, GeoRL, 1, 291
Press, W. H., Teukolsky, S. A., Vetterling, W. T., Flannery, B. P., et al. 2007, Numerical Recipes: The Art of Scientific Computing (3th ed.; Cambridge: Cambridge Univ. Press)
Prialnik, D., & Rosenberg, E. D. 2009, MNRAS, 399, L79
Rieke, G. H., Young, E. T., Engelbracht, C. W., et al. 2004, ApJS, 154, 25
Rinaldi, G., Corte, V. D., Fulle, M., et al. 2017, MNRAS, 469, S598
Rozitis, B., & Green, S. F. 2011, MNRAS, 415, 2042
Schorghofer, N. 2008, ApJ, 682, 697
Shi, J., Ma, Y., Liang, H., & Xu, R. 2019, NatSR, 9, 5492
Snodgrass, C., Jones, G. H., Boehnhardt, H., et al. 2018, AdSpR, 62, 1947
Spencer, J. R. 1990, Icar, 83, 27
Toth, I. 2000, A&A, 360, 375
Toth, I. 2006, A&A, 446, 333
Vincent, J. B., Oklay, N., Marchi, S., et al. 2015, P&SS, 107, 53
Ward, W. R. 1974, JGR, 79, 3375
Wright, E. L., Eisenhardt, P. R. M., Mainzer, A. K., et al. 2010, AJ, 140, 1868
Yu, L. L., Ip, W. H., & Spohn, T. 2019, MNRAS, 482, 4243
Zhang, X., Huang, J., Wang, T., & Huo, Z. 2019, LPI, 50, 1045